POLITECNICO
MILANO 1863

SCUOLA DI INGEGNERIA INDUSTRIALE
E DELL'INFORMAZIONE

Executive Summary of the Thesis

# Optimization of Multistage Humidification and Dehumidification Desalination Plant Using Solar Energy (Experimental and Theoretical Study)

Laurea Magistrale in Chemical Engineering - Ingegneria Chimica

**Author:** MohammadSina GhanbariPakdehi

**Advisor:** Prof. Flavio Manenti

**Co-advisor:** Prof. Iqbal M. Mujtaba - Prof. Raj Patel

**Academic year:** 2025-2026

## 1. Introduction

Freshwater scarcity is a growing global concern. Although water covers approximately 71% of the Earth's surface, less than 2.5% is freshwater, and only a small fraction of that is readily accessible. Over 40% of the global population experiences water stress, and more than 700 million people currently lack access to safe drinking water [1]. Population growth, urbanization, and climate change are intensifying this pressure, particularly in arid, coastal, and remote regions where conventional freshwater sources are insufficient or unreliable.

Desalination offers a route to supplement freshwater supply in water-stressed regions. Large-scale thermal and membrane technologies dominate global capacity but require high-pressure equipment, extensive pretreatment, or large-scale infrastructure, making them poorly suited to decentralized, small-scale applications. Humidification-dehumidification (HDH) desalination has emerged as a low-temperature, solar-compatible alternative for this niche: saline water is heated and evaporated in a humidifier, and the moisture-laden airstream is condensed in a dehumidifier to recover freshwater at ambient pressure with simple equipment [2].

## 2. Research Objectives

The aim of this thesis is to experimentally and numerically investigate the effect of condenser surface enhancement on the performance of a compact HDH desalination system, with particular focus on freshwater productivity, regime-transition behavior, and model-based optimization. The work is organized around three interconnected research pillars.

The first pillar is experimental: five systematic condenser modification scenarios were applied to the same laboratory-scale prototype and tested across a range of air velocities. These scenarios cover coil rearrangement with mesh removal (Scenario 1), localized mesh placement within the innermost coil (Scenario 2), distributed mesh between all adjacent coil pairs (Scenario 3), high-density mesh filling all inter-coil spaces (Scenario 4), and silica-gel/PVA coating of all condenser tube surfaces (Scenario 5), following the desiccant-coating methodology in the literature [3]. A baseline three-coil configuration was used as the reference case.

The second pillar is modeling: an LMTD-based dehumidifier model implemented in gPROMS and grounded in the mechanistic framework developed by Kaunga [2] was adapted to each experimental scenario using scenario-specific effective condenser lengths. The model was assessed against the full experimental dataset and extended to a two-stage configuration for parametric analysis and operating-condition optimization.
The third pillar is solar integration: a solar collector model was coupled to the two-stage process to simulate freshwater productivity across a realistic range of solar irradiation conditions, providing a basis for assessing the viability of renewable energy-driven operation.

# 3. Experimental Methodology and Results

## 3.1. Apparatus and Operating Conditions

Experiments were conducted on a laboratory-scale HDH desalination prototype located at the Engineering and Informatics Department, University of Bradford. The system was originally designed by Kaunga [2] and subsequently extended by Asghar [4]. It comprises three functional units: a water-bath heater replicating solar thermal input, a packed-column humidifier filled with gunny bag material, and a shell-and-helical-coil dehumidifier (condenser). Auxiliary instrumentation includes flow meters, thermocouples at key positions, and a variable-speed air blower. All operating conditions other than air velocity were held constant throughout: feed-water temperature of 40 °C, feed-water flow rate of 4 L $\text{min}^{-1}$, and cooling-water flow rate of 3 L $\text{min}^{-1}$. Air velocity was the sole experimental variable, ranging from approximately 3.0 to 6.5 m $\text{s}^{-1}$.
Freshwater productivity (L $\text{h}^{-1}$) was measured by timed collection. Each data point was averaged across three replicate samples (10, 20, and 30 mL), and each condition was repeated three times. The primary performance indicator is the condensate recovery ratio:

$$\text{RR} = \frac{\dot{V}_{\text{distillate}}}{\dot{V}_{\text{feed}}} \times 100\% \qquad (1)$$

where $\dot{V}_{\text{feed}} = 240$ L $\text{h}^{-1}$ is the fixed saline-water feed flow rate.

## 3.2. Condenser Modification Scenarios

The experimental baseline condenser consisted of a three-coil helical copper arrangement with a single stainless-steel mesh positioned inside the outermost coil, with a physical outer tube area of approximately 0.25 $\text{m}^2$ ($L = 6.18$ m). For the optimization program, the geometry was redesigned into a four-coil concentric configuration, increasing the physical outer tube area to 0.63 $\text{m}^2$ ($L = 15.81$ m), a 2.56-fold increase. Five modification scenarios were then applied systematically to this four-coil assembly, as summarized in Table 1.

## 3.3. Key Findings

The central finding of the experimental work is illustrated in Figure 1: distributing stainless-steel mesh throughout the inter-coil volume (Scenario 3) produced a sharp productivity transition near 5.0 m $\text{s}^{-1}$, with output rising from approximately 0.56 L $\text{h}^{-1}$ below the threshold to 3.04 L $\text{h}^{-1}$ above it, which is a factor of approximately five. Below the threshold, mesh-induced flow resistance suppresses condensation; above it, the momentum of the airstream overcomes that resistance and enhanced vapor-surface contact dominates. This regime transition is the principal novel contribution of the experimental work.
Increasing mesh density (Scenario 4) produced a transition interval of approximately 4.0–5.0 m $\text{s}^{-1}$, with consistently high-regime productivity established above 5.0 m $\text{s}^{-1}$, and raised the peak recovery ratio to 1.37%, the highest across all configurations. However, the greater mesh loading introduced notable inter-run variability in the high-velocity regime, consistent with non-uniform flow channeling through the densely packed structure.
Scenario 5 demonstrated that silica-gel/PVA coating of the tube surfaces eliminated the threshold behavior entirely. Productivity rose smoothly and monotonically from 2.098 L $\text{h}^{-1}$ at the lowest tested velocity (3.57 m $\text{s}^{-1}$) to 3.145 L $\text{h}^{-1}$ at 6.07 m $\text{s}^{-1}$, with RR exceeding 1% at all operating points. The coating comprised 34 g of silica gel and 200 g of PVA adhesive; without a PVA-only control, the improve-

Table 1: Summary of condenser modification scenarios and key experimental results. Peak values correspond to the highest air velocity tested for each scenario.

| Scenario | Description | Peak Prod. (L $h^{-1}$) | Peak RR (%) | Key Observation |
|---|---|---|---|---|
| Baseline | Three-coil, single outer-coil mesh | 0.552 | 0.230 | Narrow band (0.456–0.552); no strong velocity trend |
| Scenario 1 | Four-coil, mesh removed | 0.407 | 0.170 | Below baseline; mesh removal eliminates air-side enhancement |
| Scenario 2 | Four-coil, mesh in innermost coil | 0.505 | 0.210 | Marginal gain; localized mesh produces no step change |
| Scenario 3 | Distributed mesh between all coil pairs | 3.038 | 1.265 | Sharp nearly five times threshold jump near 5.0 m $s^{-1}$ |
| Scenario 4 | High-density mesh in all inter-coil spaces | 3.293 | 1.372 | Transition interval 4.0–5.0 m $s^{-1}$; high inter-run variability |
| Scenario 5 | Silica-gel/PVA coating (Sc. 4 geometry) | 3.145 | 1.311 | Threshold eliminated; smooth monotonic response at all velocities |

ment is attributed to the composite coating as a whole rather than to silica gel alone.

# 4. Mathematical Modeling and gPROMS Simulation

## 4.1. Model Framework

The dehumidifier model is based on the log-mean temperature difference (LMTD) method, which relates the heat transfer rate to an overall heat transfer coefficient, an effective condenser area, and the terminal temperature driving force between the vapor and coolant streams:

$$Q = U_{\mathrm{ov}}\, A_c\, \Delta T_{\mathrm{lm}} \tag{2}$$

where $\Delta T_{\mathrm{lm}}$ is defined as:

$$\Delta T_{\mathrm{lm}} = \frac{\Delta T_1 - \Delta T_2}{\ln(\Delta T_1/\Delta T_2)} \tag{3}$$

$$\Delta T_1 = T_v^{\mathrm{in}} - T_c^{\mathrm{out}} \tag{4}$$

$$\Delta T_2 = T_v^{\mathrm{out}} - T_c^{\mathrm{in}} \tag{5}$$

The overall heat transfer coefficient $U_{\mathrm{ov}}$ accounts for vapor-side, tube-wall, and cooling-water resistances in series. The governing equations were adopted from the mechanistic framework developed by Kaunga and implemented in gPROMS ModelBuilder as a coupled humidifier-dehumidifier system [2]. The humidifier model describes countercurrent heat and mass transfer in a packed bed (gunny-bag packing in the present prototype; the model structure and correlations are inherited from Kaunga's Raschig-ring framework), while the dehumidifier model uses Equations (2) and (3) together with a vapor condensation rate expression to predict freshwater productivity and RR.

The effective condenser heat transfer area $A_c$ is related to an effective tube length $L$ through $A_c = \pi d_o L$, where $d_o$ is the outer tube diameter. This parameter is the primary fitting variable: adjusting $L$ scenario-by-scenario encodes geometric and surface changes without modifying the underlying model equations. Because $A_c$ is derived from $L$, the quantities $U_{\mathrm{ov}}$ and $A_c$ are mutually confounded and cannot be identified independently; the apparent thermal conductance $U_{\mathrm{ov}}A_c$ is therefore the appropriate cross-scenario diagnostic.

## 4.2. Scenario-Specific Effective Length and Assessment Results

The experimental baseline (three-coil with mesh) was assigned $L = 6.18$ m, corresponding to its physical outer tube area of 0.25 $m^2$.

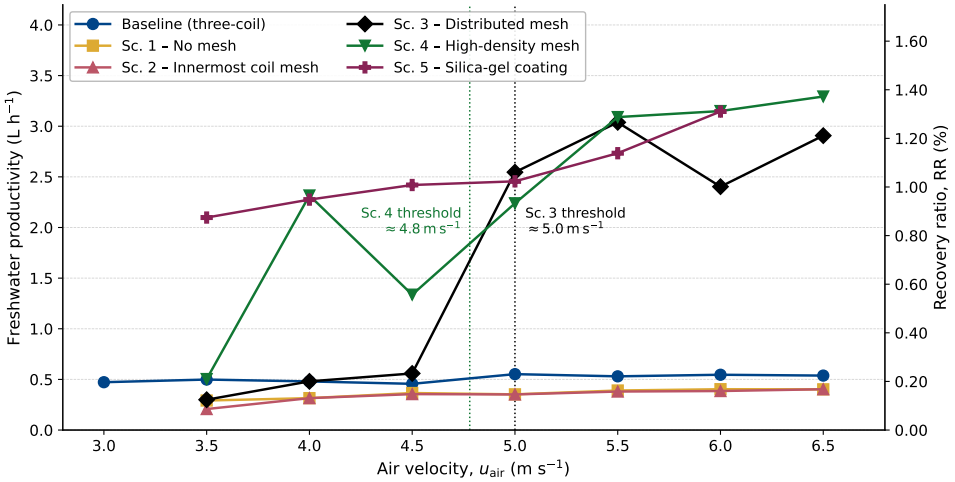


Figure 1: Freshwater productivity as a function of air velocity for all condenser configurations. The shaded region marks the Scenario 4 transition interval (4.0–5.0 m $s^{-1}$). Error bars represent one standard deviation of three repeat measurements.

Single-regime four-coil configurations (Scenarios 1 and 2) were assigned $L = 15.81$ m. The gPROMS model reproduced these scenarios with mean absolute errors (MAE) of 6.6%, 8.9%, and 9.7% respectively under a boundary-condition-assisted assessment framework, in which the dehumidifier inlet vapor pressure was reconstructed from the measured condensate rate rather than measured directly.

Threshold configurations required a velocity-dependent switching strategy. Below the threshold velocity $u^*$, the effective area remains close to the baseline; above it, the mesh-assisted condensation regime activates a substantially larger wetted area. This is encoded as:

$$L = \begin{cases} L_{\text{low}} & u_g < u^* \\ L_{\text{high}} & u_g \geq u^* \end{cases} \tag{6}$$

For Scenario 3, $L_{\text{high}} = 90.50$ m with $u^* \approx 5.0$ m $s^{-1}$, yielding MAE = 15.5% after excluding the transition-zone run. For Scenario 4, $L_{\text{high}} = 93.65$ m with $u^* \approx 4.03$ m $s^{-1}$ (the lower bound of the transition interval), yielding MAE = 10.1% after excluding one transition-zone run and one boundary-condition anomaly; the all-point MAE was 34.7%. Scenario 5, where the silica-gel/PVA coating eliminated threshold behavior entirely, was assigned a single fixed $L = 93.65$ m, giving MAE = 16.3%. Model assessment results are consolidated in Table 2.

Table 2: gPROMS model assessment: effective tube length and MAE per scenario. MAE values for Scenarios 3 and 4 exclude transition-zone and anomalous runs.

| Scenario | $L$ (m) | MAE (%) |
|---|---|---|
| Exp. baseline | 6.18 (fixed) | 6.6 |
| Scenario 1 | 15.81 (fixed) | 8.9 |
| Scenario 2 | 15.81 (fixed) | 9.7 |
| Scenario 3 | 15.81 / 90.50 (switch) | 15.5 |
| Scenario 4 | 15.81 / 93.65 (switch) | 10.1[a] |
| Scenario 5 | 93.65 (fixed) | 16.3 |

[a] After excluding one transition-zone run and one boundary-condition anomaly.

The fitted $U_{\text{ov}}$ values revealed an important diagnostic: mesh-enhanced scenarios returned lower $U_{\text{ov}}$ values than the no-mesh configurations, not because their thermal performance was weaker, but because the condensation duty was distributed over a much larger effective area. The apparent thermal conductance $U_{\text{ov}}A_c$ increased monotonically from Scenario 1 through Scenario 5, consistent with the experimental productivity ranking.

## 5. Two-Stage Optimization and Solar Integration

### 5.1. Two-Stage Model Configuration

The validated single-stage model was extended to a two-stage configuration by connecting a sec-

ond humidifier-dehumidifier pair in series. The brine outlet of Stage 1 feeds Stage 2 as its liquid inlet, allowing residual moisture content to be partially recovered. The Stage 1 evaporation ratio $ER_1$, defined as:

$$ER_1 = \frac{W(L)\,\dot{m}_g}{\dot{m}_w} \times 100\% \tag{7}$$

where $W(L)$ is the humidifier outlet humidity ratio (kg vapor per kg dry air), serves as the optimization objective. The fraction of feed water evaporated by the humidifier differs from the condensate recovery ratio RR; total condensate recovery $RR_{\text{total}} = (\dot{m}_{c,1} + \dot{m}_{c,2})/\dot{m}_w \times 100\%$ is reported alongside it. Three operating variables were selected as decision variables: feed-water inlet temperature $T_{w,\text{in}}$, air mass flow rate $\dot{m}_g$, and water mass flow rate $\dot{m}_w$.

## 5.2. Parametric Study

Feed-water temperature was the dominant operating variable. Increasing $T_{w,\text{in}}$ from 60 to 75 °C raised $ER_1$ from 4.42% to 9.20%, reflecting the exponential dependence of the saturation vapor pressure on temperature, which amplifies the humidity-ratio driving force in the humidifier. Air mass flow rate had a strong positive effect, with $ER_1$ rising from 4.42% to 8.64% as $\dot{m}_g$ increased from 0.50 to 1.00 kg $s^{-1}$; the system became infeasible at 1.50 kg $s^{-1}$ due to the humidifier energy-balance limit. Water mass flow rate showed a non-monotonic response: $ER_1$ peaked at 6.05% at $\dot{m}_w = 2.0$ kg $s^{-1}$ and declined at higher liquid loading, consistent with flooding-driven suppression of mass transfer in the packed bed.

## 5.3. Optimization Results

The optimization was solved using the gPROMS CVP_SS–SQP framework. The best feasible operating point was identified at $T_{w,\text{in}} = 70.1$ °C, $\dot{m}_g = 0.849$ kg $s^{-1}$, and $\dot{m}_w = 1.4$ kg $s^{-1}$. At this point, $ER_1$ increased from 4.42% to 12.13%, a 174% improvement over the baseline, accompanied by a reduction in Stage 2 evaporation ratio from 1.74% to 0.75%. Total condensate recovery $RR_{\text{total}}$ increased from 5.96% to approximately 12.9%. The result is reported as a feasible best point within the prescribed bounds rather than a confirmed global optimum, because the stationarity convergence criterion was not fully satisfied.

## 5.4. Solar Collector Integration

The two-stage process was coupled to an evacuated-tube solar collector model and a shell-and-tube heat exchanger, replacing the fixed $T_{w,\text{in}}$ boundary condition with a solar-driven thermal supply. The collector efficiency follows the second-order model:

$$\eta_c = \eta_o - a_c \frac{T_m - T_{\text{amb}}}{I_T} - b_c \left( \frac{T_m - T_{\text{amb}}}{I_T} \right)^2 \tag{8}$$

where $I_T$ is the incident solar irradiation, $T_m$ is the mean heat-transfer fluid temperature, and $\eta_o$, $a_c$, $b_c$ are optical and heat-loss coefficients taken from Kaunga [2]. The collector aperture area was set to 742 $m^2$, consistent with the multistage solar case in that reference.
Solar irradiation was swept from 300 to 540 W $m^{-2}$. The key results are summarized in Table 3 and Figure 2.

Table 3: Solar-integrated simulation results across the irradiation sweep. All parameters other than $I_T$ held at optimised values.

| $I_T$ (W $m^{-2}$) | $T_{w,\text{in}}$ (°C) | $ER_1$ (%) | $\dot{m}_{c,\text{total}}$ (kg $s^{-1}$) |
|---|---|---|---|
| 300 | 48.7 | 4.21 | 0.034 |
| 350 | 53.8 | 5.44 | 0.055 |
| 400 | 58.9 | 7.00 | 0.092 |
| 450 | 63.9 | 8.98 | 0.157 |
| 500 | 69.0 | 11.50 | 0.276 |
| 540 | 73.1 | 14.00 | 0.428 |

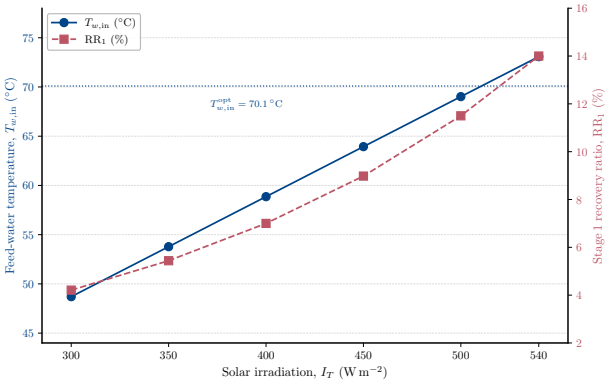


Figure 2: Feed-water inlet temperature $T_{w,\mathrm{in}}$ (navy circles, left axis) and Stage 1 evaporation ratio $ER_1$ (crimson squares, right axis) as a function of solar irradiation $I_T$. The horizontal dotted line marks the optimised feed-water temperature of 70.1 °C.

Feed-water temperature increased linearly with irradiation, rising from 48.7 °C at 300 W m$^{-2}$ to 73.1 °C at 540 W m$^{-2}$. $ER_1$ responded nonlinearly, increasing from 4.21% to 14.00% over the same range, with the rate of change accelerating at higher irradiation levels due to the thermodynamic nonlinearity of the humidification process. Total freshwater production increased approximately 13-fold across the sweep, from 0.034 to 0.428 kg s$^{-1}$. At the base-case irradiation of 450 W m$^{-2}$, the model yields approximately 13.6 m$^3$ d$^{-1}$, consistent with solar-HDH systems of comparable collector area reported in the literature [2]. Collector efficiency increased monotonically from 0.626 to 0.706 across the sweep, consistent with evacuated-tube collector behavior at increasing irradiation. The upper feasibility limit of 540 W m$^{-2}$ arises from the reversal of the Stage 2 condensation driving force at higher feed-water temperatures.

## 6. Conclusions

This thesis investigated condenser surface enhancement and process optimization for a compact HDH desalination prototype through five experimental scenarios, gPROMS-based LMTD modelling, and solar-integrated two-stage simulation. The following conclusions are drawn.

Mesh spatial distribution governs productivity in the helical-coil condenser. Distributing mesh between all inter-coil pairs (Scenario 3) produced a nearly 5-fold productivity jump near 5.0 m s$^{-1}$, from 0.56 to 3.04 L h$^{-1}$, representing the principal novel experimental finding. Silica-gel/PVA coating (Scenario 5) eliminated this threshold, sustaining RR above 1% across all velocities with reduced variability. Coil rearrangement without mesh reduced productivity below the baseline.

The LMTD model reproduced single-regime scenarios with MAE of 6.6% to 9.7%. Scenarios 3 and 4 required velocity-dependent effective-length switching, achieving MAE of 15.5% and 10.1% respectively outside the transition zone; Scenario 5 used a single fixed effective length and achieved MAE of 16.3%. The apparent thermal conductance $U_{\mathrm{ov}}A_c$ is the appropriate cross-scenario diagnostic when effective area varies between configurations.

Two-stage optimization identified a best feasible point at $T_{w,\mathrm{in}} = 70.1\,°C$, $\dot{m}_g = 0.849$ kg s$^{-1}$, and $\dot{m}_w = 1.4$ kg s$^{-1}$, improving Stage 1 evaporation ratio $ER_1$ from 4.42% to 12.13% (+174%) and total condensate recovery from 5.96% to approximately 12.9%. Solar integration confirmed that this operating condition is achievable at 520 W m$^{-2}$, with total freshwater production increasing 13-fold across the 300 to 540 W m$^{-2}$ irradiation range, supporting the viability of renewable-driven compact HDH for decentralized applications.

## References

[1] Hilla Shemer, Shlomo Wald, and Raphael Semiat. Challenges and Solutions for Global Water Scarcity. *Membranes*, 13(6), 2023.

[2] Damson Leonard Kaunga. *Modelling, Simulation and Optimisation of Multistage Humidification and Dehumidification Desalination Plant Using Solar Energy.* Doctor of Philosophy (PhD), University of Bradford, Bradford, United Kingdom, 2022.

[3] T. S. Ge, Y. J. Dai, R. Z. Wang, and Z. Z. Peng. Experimental comparison and analysis on silica gel and polymer coated fin-tube heat exchangers. *Energy*, 35(6):2893–2900, 2010.

[4] Ghayas Asghar. *Optimisation of Humidification-Dehumidification Desalination Process.* MSc Dissertation, University of Bradford, 2022.